JOURNAL OF THEORETICAL AND APPLIED MECHANICS
63, 1, pp. 51-58, Warsaw 2025
https://doi.org/10.15632/jtam-pl/194239

PIEZORESISTIVE SENSING MECHANISM OF GRAPHENE-BASED ELECTRONIC SKIN

Li Li
Department of Dermatology, Xi'an No.3 Hospital, Xi'an, PR China, and
The Affiliated Hospital of Northwest University, Xi'an, PR China
Jia Huang
Xi'an University of Technology, Xi'an, PR China
Wenbin Yang
Department of Dermatology, Xi'an No.3 Hospital, Xi'an, PR China, and
The Affiliated Hospital of Northwest University, Xi'an, PR China
e-mail: YangWB0910@126.com

The graphene-based sensing electronic skin has a broad application prospect, but its piezoresistive sensing mechanism still needs to be further studied. In this work, according to the microscopic characteristics of the graphene electronic skin, the Monte Carlo stochastic algorithm is used to generate randomly distributed graphene sheets, and then the piezoresistive sensor model of the graphene electronic skin is established. The relative resistance and gauge factor of the model are calculated by the finite element method. Meanwhile, the current density and potential contour under different graphene morphology are obtained. The results show that the graphene sensor with a high area fraction has a higher sensing range, and the graphene sensor with a low area fraction has a higher gauge factor. The piezoresistive effect of the model depends mainly on a change of graphene sheet density. With the change of strain, the variation of the overlap area and overlap number between graphene sheets will cause a change of graphene density and electron migration path. The separation between graphene sheets can lead to reduction in electron migration paths, resulting in nonlinear changes in the relative resistance of the model. The present work can provide technical support for design and preparation of the graphene-based electronic skin.

Keywords: graphene, electronic skin, finite element method, piezoresistive effect

1. Introduction

Skin is the largest organ of the human body, and it is a multi-functional sensor that can clearly perceive changes in the external environment, which is of great significance to the survival and development of human beings. Electronic skin, on the other hand, is a device that simulates the function of human skin (Ma and Khoo, 2024; Li *et al.*, 2023; Guo *et al.*, 2024; Fang *et al.*, 2021). It can mimic the tactile sensing function and flexible performance of human skin, and can attach to the surface of human skin or robots, sensing various stimuli such as pressure, temperature, etc. It has shown broad application prospects in fields such as intelligent medicine, human prosthetics, and health monitoring (Mudhulu *et al.*, 2023; Xiao *et al.*, 2023; Xu *et al.*, 2023; Hu *et al.*, 2024; Liao *et al.*, 2024).

The piezoresistive sensing electronic skin based on graphene has gained great attention due to its excellent sensitivity and flexibility (Chen *et al.*, 2023b; Fang *et al.*, 2023; Chen *et al.*, 2023c; Chen *et al.*, 2023a). Yun *et al.* (2023) prepared a waterproof and ultra sensitive wearable strain sensor using carbon black/graphene/carboxymethyl cellulose, which can easily capture signals

of spatial strain during body movement. Feng *et al.* (2023) reported a new type of graphene-based resistance sensor with high sensitivity and response speed, and its blood pressure detection error value has passed the standards of the Association for the Advancement of Medical Instrumentation standard. Sharma *et al.* (2023) proposed a piezoresistive sensor based on graphene nanosheets and a PDMS substrate, which can detect both fine and large strains with good stability and repeatability. Wei *et al.* (2021) prepared a wearable piezoresistive sensor with high sensing performance through polypyrrole and reduced graphene aerogel. Hong *et al.* (2024) successfully prepared a dual biomimetic stretchable strain sensor with fingerprint patterns and a biomimetic lotus root fiber structure using silicone rubber, multi walled carbon nanotubes, and graphene, which could accurately achieve gesture recognition, human micro-expression monitoring. Combined with machine-learning algorithms, Ma *et al.* (2923) proposed a porous graphene-based flexible pulse sensor for cardiovascular disease diagnostics, which achieves high accuracy ($> 93\%$), showing a broad application prospect of the electronic skin.

In order to establish the connection between the macroscopic performance and microscopic structure of graphene-based composite sensors, and to study their sensing mechanism at a deeper level, numerical simulation is an economically effective method. Li and Yang (2020) established a two-dimensional random model through theoretical modeling and finite element simulation to study the piezoresistive behavior of stacked graphene composite sensors. Ren *et al.* (2022) used the finite element method to analyze the mechanical stress and deflection of the graphene piezoresistors, established a functional relationship between mechanical properties and size variables, and determined the optimal size of the structure. Lamba *et al.* (2022) used finite element analysis to design and simulate graphene piezoresistive sensors, which had the ability to perceive biaxial forces and were therefore suitable for microbiology, minimally invasive surgery, and healthcare applications.

In the present work, we establish a two-dimensional sensor model based on the microstructure characteristics of the graphene-based electronic skin, and explore the piezoresistive sensing mechanism of the graphene-based electronic skin and the influence of microstructure parameters on piezoresistive performance.

2. Graphene-based electronic skin sensing model

Based on the structural characteristics of randomly stacked graphene sheets in electronic skin (Li *et al.* (2016), the Monte Carlo random algorithm is used to generate randomly distributed graphene sheets, as shown in Fig. 1.

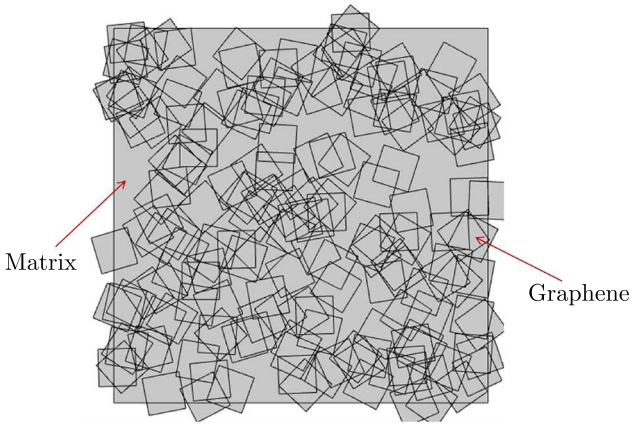

Fig. 1. Schematic diagram of the graphene sensor model

This work makes the following assumption: Firstly, since the modulus of graphene is much larger than that of the matrix, we can consider graphene sheets as rigid materials. Secondly, due to significant van der Waals forces between graphene sheets and polymer matrix materials, it is assumed that the matrix can fully transfer deformation to the graphene sheets. Finally, it is assumed that the sensor has uniform deformation, meaning that the center of the graphene sheet remains unchanged relative to the entire sensor position. If the model extends along the x-direction, the center coordinates of the i-th graphene at any time can be expressed as

$$x_i = x_i^0(1+\varepsilon) \qquad y_i = y_i^0(1-\nu\varepsilon) \tag{2.1}$$

where ε is the linear strain along the x-direction of the model, and ν is Poisson's ratio of the matrix material.

Commonly used electronic skin generally takes rubber as the matrix material. Under a large deformation, in order to determine Poisson's ratio of rubber, a small unit is taken out with an initial volume of $V_0 = dx\,dy\,dz$. The volume of the unit after deformation at unidirectional stress σ_x is $V_1 = (1+\varepsilon)(1-\nu\varepsilon)^2\,dx\,dy\,dz$. Due to the incompressibility of rubber, there is

$$1 = (1+\varepsilon)(1-\nu\varepsilon)^2 \tag{2.2}$$

Solving equation (2.2) yields

$$\nu = \frac{1}{\varepsilon} \pm \frac{1}{\varepsilon\sqrt{1+\varepsilon}} \tag{2.3}$$

Because $1-\varepsilon$ is greater than zero, the negative sign is taken from Eq. (2.3), which means that Poisson's ratio of rubber is

$$\nu = \frac{1}{\varepsilon} - \frac{1}{\varepsilon\sqrt{1+\varepsilon}} \tag{2.4}$$

Based on Eq. (2.1), we can rewrite the central coordinates of the i-th graphene sheet as

$$x_i = x_i^0(1+\varepsilon) \qquad y_i = y_i^0\frac{1}{\sqrt{1+\varepsilon}} \tag{2.5}$$

In order to analyze the resistance changes of the graphene sensor model, the left and right ends of the model are used as two electrodes, with constant current input and output respectively. Therefore, the analysis of resistance is transformed into the solution of the following control equation

$$\nabla \cdot J = Q_{j,V} \qquad J = \sigma E + J_e \qquad E = -\nabla V \tag{2.6}$$

where J represents current density, E represents electric field intensity, V represents electric potential, σ is electrical conductivity, $Q_{j,v}$ is an external current source, and J_e is the externally generated current density.

The boundary conditions of this model are insulation between the upper and lower boundaries, with terminals on the left and grounding on the right boundary. The basic solution approach is to use the finite element method to obtain the potential and current distribution of the model, and then use Ohm's law to determine the model resistance. The numerical calculations are performed with the COMSOL Multiphysics Software.

The above methods can be used to study the piezoresistive performance of graphene sensors. The gauge factor β is an important indicator for judging the piezoresistive performance of sensors, which represents the relative resistance per unit strain, i.e.

$$\beta = \frac{\Delta R}{R\varepsilon} \tag{2.7}$$

When the gauge factor β is a constant a indicates that the relative resistance varies linearly with strain, and the graphene sensor outputs a linear signal. Conversely, the sensor outputs a nonlinear signal.

3. Results and discussion

In this work, the electrical resistivity of single-layer graphene $\rho_0 = 4.2 \cdot 10^{-8}\,\Omega$m, and the in-plane resistivity of the overlapping area of multi-layer graphene sheets is equal to the parallel value of the resistances of each single-layer graphene sheet, i.e ρ_0/n, where n is the number of layers of graphene stacking. The resistivity of the rubber matrix is $1 \cdot 10^{13}\,\Omega$m, which is much higher than the resistivity of graphene. In the model, the content of graphene is represented by the area fraction $f = mA/A_0$, where m is the number of graphene sheets, A is the area of each graphene sheet, and A_0 is the area of the model.

Figure 2 shows the variation of the relative resistance and gauge factor of sensors with strain under different GNPs area fraction. The simulation results shown in Fig. 2a indicate that the initial stage of relative resistance changes approximately linearly, and as the strain increases, the resistance begins to increase rapidly. Because when the strain starts to increase, the GNPs mainly slips, causing only an increase in the length of the electron migration path. But when the deformation is large, the GNPs begin to separate, and the number of graphene sheets that do not participate in current transfer increases, reducing the electron migration path, resulting in a sudden change in relative resistance. Due to the larger slip range between graphene sheets with a high area fraction, the relative resistance of graphene sensors with the high area fraction will also exhibit better linear performance when the model is extended. At the same time, it can be seen that the sensing range of the high area fraction graphene sensor is higher, mainly due to better connectivity of the high aspect ratio graphene sensor when the model is extended. From Fig. 2b, it can be seen that sensors with a lower area fraction have a higher gauge factor, because for graphene sensors with lower area fraction, the increase in resistance caused by separation of graphene sheets can be more easily reflected. The above simulation results are consistent with the experimental conclusions of Son *et al.* (2019) and Sethy *et al.* (2019), which confirms that this model can simulate the piezoresistive effect of the graphene-based electronic skin.

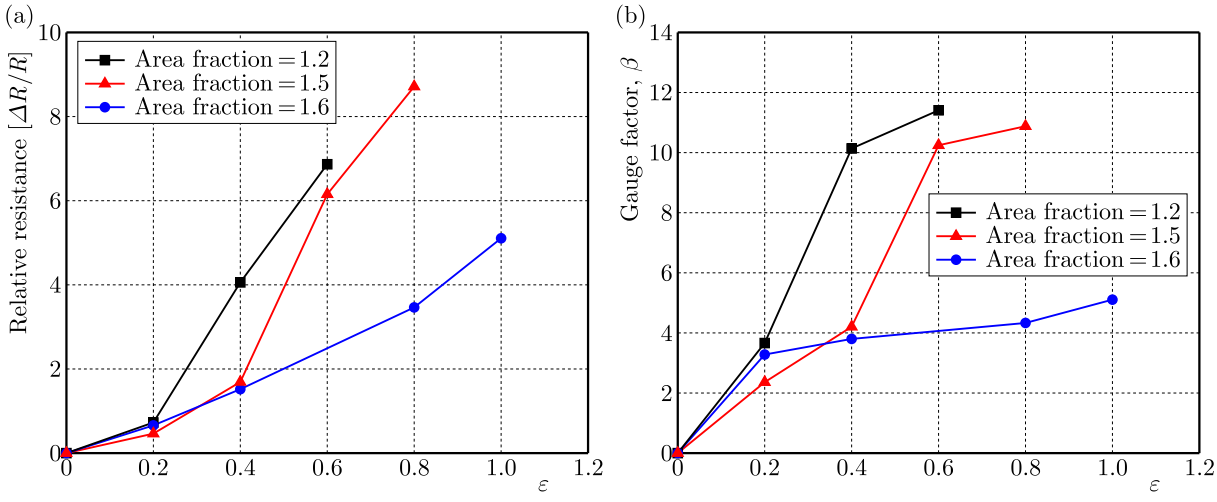

Fig. 2. Relative resistance $\Delta R/R$ and gauge factor β under different strains

Figure 3 shows the contour of current density under different strains. By observing Fig. 3a, three network branches with high current density are formed respectively at the upper, middle and lower positions of the sensor model. The low current density region in the model includes not only the rubber substrate (the rubber matrix has very low electrical conductivity, so the current density value is low), but also the graphene sheets separated from the network, which can be regarded as invalid sheets. Figure 3b shows the current density at a strain of 0.2, which forms two high current density network branches in the upper and middle positions of the model, reducing one branch compared to Fig. 3a. This indicates that the current density in the lower branch

plummets, and the graphene sheet in the branch also becomes an ineffective sheet that does not participate in electron transfer, due to the separation of the graphene sheet in the lower branch. By comparing Fig. 3b and Fig. 3c, we find that the network branch in the middle region is also disconnected, which is manifested as a sharp drop in the current density in the middle region. The strain range from 0.2 to 0.4 not only involves the separation of longitudinal graphene sheets, but also the connection of transverse graphene sheets. Observing Figs. 3b and 3c, the current density originally located in the middle region of the left end has not been very high. However, due to the increase in strain, the graphene sheet appears to be getting closer and closer horizontally. Finally, when the strain is 0.4, the graphene sheet forms an electron migration channel in the horizontal direction. When the strain continued to increase to 0.6, as the graphene sheet separated, only a high current density electron migration path remained above the model.

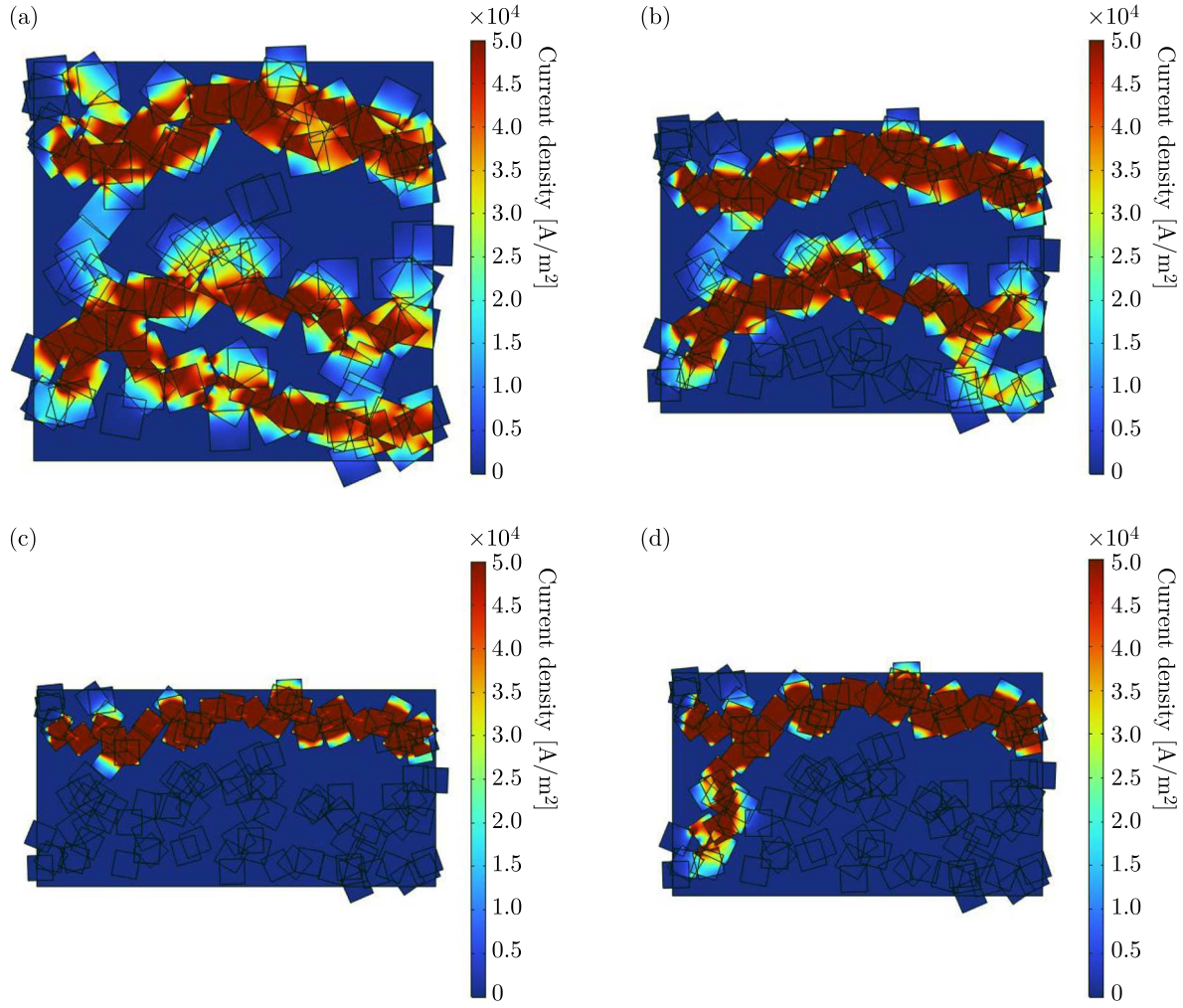

Fig. 3. Current density contour under different strains: (a) $\varepsilon = 0$, (b) $\varepsilon = 0.2$, (c) $\varepsilon = 0.4$, (d) $\varepsilon = 0.6$

Taking the model with an area fraction of 1.2 as an example, Fig. 4 shows the potential contour under different strains. When the strain is 0, it is basically in the low potential region. As shown in Fig. 3, at this time, there are more parallel branches and smaller resistance. But when the strain is increased to 0.2, the high potential region significantly increases, mainly because with the increase of strain, the graphene sheet begins to gradually slip, and the overlapping area of graphene gradually decreases, leading to a gradual increase in resistance. When the strain reaches 0.4, as the electron migration path decreases, the low potential region increases. However, the potential value in the high potential region increased, mainly due to the further

increase in resistance with the slip of graphene. When the strain increcases to 0.6, this trend becomes more pronounced.

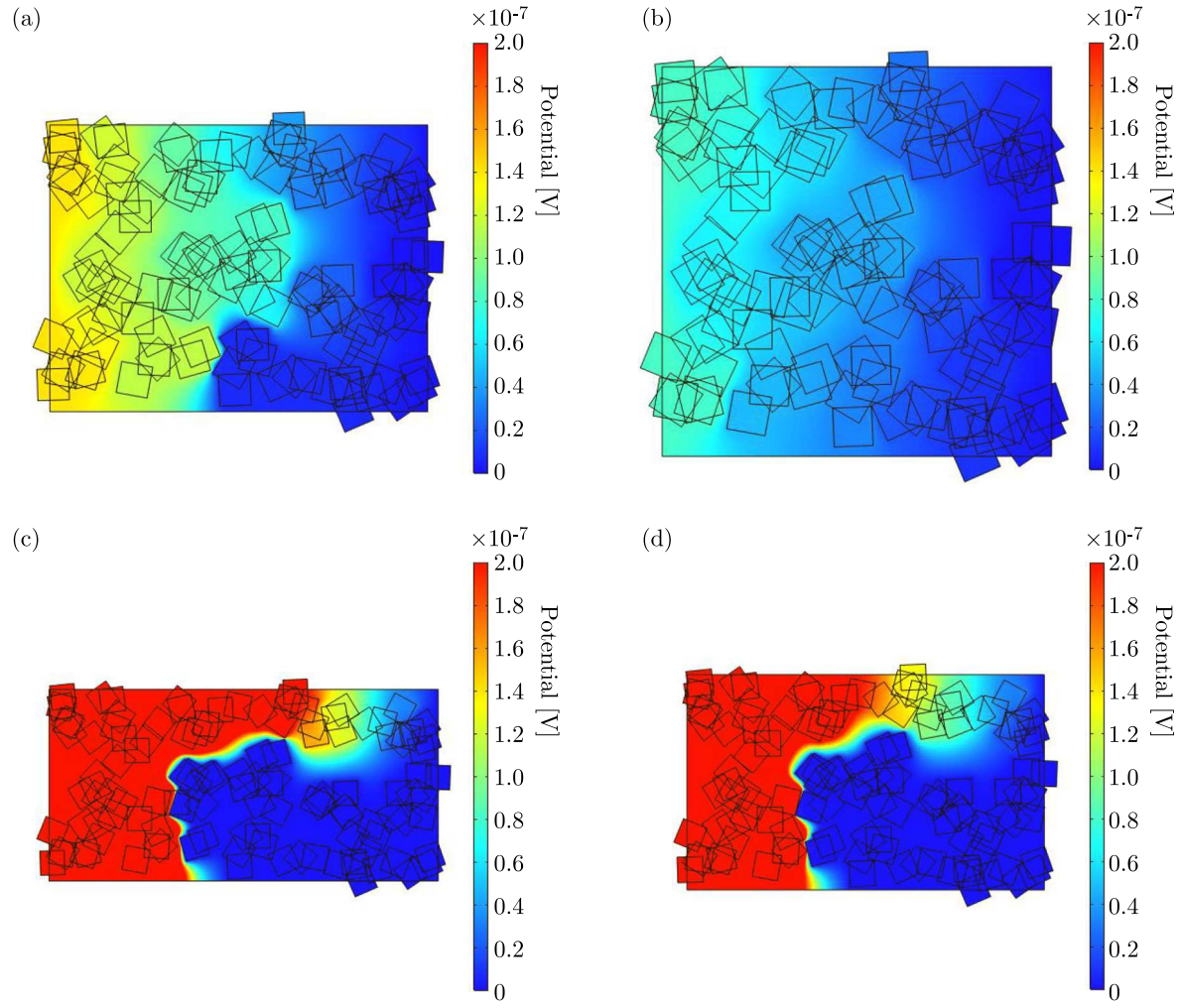

Fig. 4. Potential contour under different strains: a) $\varepsilon = 0$, (b) $\varepsilon = 0.2$, (c) $\varepsilon = 0.4$, (d) $\varepsilon = 0.6$

It should be noted that in addition to the morphological changes of graphene sheets (relative slip and separation of overlapping graphene sheets) affecting the piezoresistive properties of electronic skin, the tunneling effect between graphene sheets also has an impact on it (Wu *et al.*, 2019; Liu *et al.*, 2016). However, the sensing range where the tunneling effect plays a role is only a few nanometers. For graphene-based composites that can sense large deformations, the contribution of the tunneling effect to the piezoresistive performance of composites is very small. Therefore, to maintain simplicity of the model, the present work does not consider the influence of the tunneling effect on the piezoresistive performance of the graphene-based electronic skin.

4. Conclusions

The present work establishes a piezoresistive sensor model of the graphene-based electronic skin using a Monte Carlo random algorithm and finite element method. The results show that graphene-based sensors with a low area fraction have a higher gauge factor, while graphene sensors with a high area fraction have a higher sensing range. By comparing the current density and potential contour of different graphene morphology, it can be seen that the piezoresistive effect

of the sensor mainly depends on the change in graphene sheet density. The initial deformation of the graphene sensing model is dominated by the slip of graphene, during which the resistance changes linearly. As the strain increases to a certain extent, the graphene sheets begin to separate, leading to a decrease in the network path and causing a sudden change in the resistance of the model (i.e. non-linear change).

References

1. Chen H., Zhuo F.L., Zhou J., Liu Y., Zhang J.B., *et al.*, 2023a, Advances in graphene-based flexible and wearable strain sensors, *Chemical Engineering Journal*, **464**, 142576
2. Chen K., Xu Y., Zhao Y., Li J., Wang X., Qu L.T., 2023b, Recent progress in graphene-based wearable piezoresistive sensors: From 1D to 3D device geometries, *Nano Materials Science*, **5**, 3, 247-264
3. Chen X.X., Yin Z.Z., Deng Y.T., Li Z.H., Xue M.S., *et al.*, 2023c, Harsh environment--tolerant and robust superhydrophobic graphene-based composite membrane for wearable strain sensor, *Sensors and Actuators A: Physical*, **362**, 114630
4. Fang H.Q., Yao D.H., Gao X.P., Sun Y.F., Shiwei A., *et al.*, 2023, Flexible sensors with tannin-modified vertical graphene arrays for the highly sensitive detection of humidity and strain, *Sensors and Actuators A: Physical*, **352**, 114213
5. Fang Y.S., Zou Y.J., Xu J., Chen G.R., Zhou Y.H., *et al.*, 2021, Ambulatory cardiovascular monitoring via a machine-learning-assisted textile triboelectric sensor, *Advanced Materials*, **33**, 41, 2104178
6. Feng H., Liu P., Guo X., Li J.L., Sun Y.F., *et al.*, 2023, PSS modified by 3-aminopropyltrimethoxysilane linking large-area GNPs/PSS to silicone rubber with stable interface combination for high sensitivity flexible resistive sensor, *Chemical Engineering Journal*, **465**, 143009
7. Guo W., Ma Z.Q., Chen Z., Hua H.J., Wang D., *et al.*, 2024, Thin and soft Ti_3C_2Tx MXene sponge structure for highly sensitive pressure sensor assisted by deep learning, *Chemical Engineering Journal*, **485**, 149659
8. Hong W.Q., Guo X.H., Zhang T.X., Zhu X.W., Su Z., *et al.*, 2024, Dual bionic-inspired stretchable strain sensor based on graphene/multi-walled carbon nanotubes/polymer composites for electronic skin, *Composites Part A: Applied Science and Manufacturing*, **179**, 108043
9. Hu X.H., Ma Z.Q., Zhao F.Q., Guo S., 2024, Recent advances in self-powered wearable flexible sensors for human gaits analysis, *Nanomaterials*, **14**, 1173
10. Lamba M., Chaudhary H., Singh K., Keshyep P., Kumar V., 2022, Graphene piezoresistive flexible MEMS force sensor for bi-axial micromanipulation applications, *Microsystem Technologies*, **28**, 7, 1687-1699
11. Li J., Jia H.L., Zhou J.K., Huang X.C., Xu L., *et al.*, 2023, Thin, soft, wearable system for continuous wireless monitoring of artery blood pressure, *Nature Communications*, **14**, 5009
12. Li X.M., Yang T.T., Yang Y., Zhu J., Li L., *et al.*, 2016, Large-area ultrathin graphene films by single-step Marangoni self-assembly for highly sensitive strain sensing application, *Advanced Functional Materials*, **26**, 9, 1322-1329
13. Li Z., Yang Q.S., 2020, Sensing mechanism of flexible and stretchable composites based on stacked graphene, *Materials and Design*, **187**, 108384
14. Liao J.C., Ma Z.Q., Liu S.Y., Li W., Yang X.D., *et al.*, 2024, Programmable microfluidic--assisted highly conductive hydrogel patches for customizable soft electronics, *Advanced Functional Materials*, **34**, 41, 2401930
15. Liu Y., Zhang D., Wang K., Liu Y.Y., Shang Y., 2016, A novel strain sensor based on graphene composite films with layered structure, *Composites Part A: Applied Science and Manufacturing*, **80**, 95-103

16. Ma Z.Q., Hua H.J., You C.X., Ma Z.H., Guo W., *et al.*, 2023, FlexiPulse: A machine-learning-enabled flexible pulse sensor for cardiovascular disease diagnostics, *Cell Reports Physical Science*, **4**, 12, 101690

17. Ma Z.Q., Khoo B.L., 2024, Recent advances in laser-induced-graphene-based soft skin electronics for intelligent healthcare, *Soft Science*, **4**, 26

18. Mudhulu S., Channegowda M., Balaji S., Khosla A., Sekhar P., 2023, Trends in graphene-based e-skin and artificial intelligence for biomedical applications – A review, *IEEE Sensors Journal*, **23**, 17, 18963-18976

19. Ren X.C., Liu X.Y., Su X., Jiang X.F., 2022, Design and optimization of a pressure sensor based on serpentine-shaped graphene piezoresistors for measuring low pressure, *Sensors*, **22**, 13, 4937

20. Sethy D., Makireddi S., Varghese F.V., Balasubramaniam K., 2019, Piezoresistive behaviour of graphene nanoplatelet (GNP)/PMMA spray coated sensors on a polymer matrix composite beam, *Express Polymer Letters*, **13**, 11, 1018-1025

21. Sharma P., Sharma R., Janyani V., Verma D., 2023, Development of a multi-modal graphene nanoparticles (GNP)-Polydimethylsiloxane (PDMS) flexible sensor for human activity monitoring and health assessment, *International Journal of Electrochemical Science*, **18**, 9, 100236

22. Son W., Kim K., Lee S., Hyeon G., Hwang K.G., Park W., 2019, Ecoflex-passivated graphene-yarn composite for a highly conductive and stretchable strain sensor, *Journal of Nanoscience and Nanotechnology*, **19**, 10, 6690-6695

23. Wei H.G., Li A., Kong D.S., Li Z.Z., Cui D., *et al.*, 2021, Polypyrrole/reduced graphene aerogel film for wearable piezoresisitic sensors with high sensing performances, *Advanced Composites and Hybrid Materials*, **4**, 1, 86-95

24. Wu S., Peng S., Yu Y., Wang C., 2019, Strategies for designing stretchable strain sensors and conductors, *Advanced Materials Technologies*, **5**, 2, 1900908

25. Xiao Y.C., Chen Q.L.,Yang Z.M., Xi M., Zhao Y.L., *et al.*, 2023, Asymmetric and skin-mimicking hydrogels with wide temperature tolerance and superior elasticity for high-performance strain sensors, *ACS Omega*, **8**, 49, 46676-46684

26. Xu Q.Y., Li M.M., Zhang Y.X., Gao H.G., Zhang L., *et al.*, 2023, Super anti-freezing, fast-responsive nanocomposite organohydrogels with excellent mechanical properties as multifunctional sensors for human motion monitoring, *Polymer*, **283**, 126248

27. Yun T.T., Du J., Ji X.X., Tao Y.H., Cheng Y., *et al.*, 2023, Waterproof and ultrasensitive paper-based wearable strain/pressure sensor from carbon black/multilayer graphene/carboxymethyl cellulose composite, *Carbohydrate Polymers*, **313**, 120898

Manuscript received June 7, 2024; accepted for publication October 7, 2024